

Full Length Article

Effect of post-treated low-temperature plasma nitriding on the wear and corrosion resistance of 316L stainless steel manufactured by laser powder-bed fusion



M. Godec*, Č. Donik, A. Kocijan, B. Podgornik, D.A. Skobir Balantič

Institute of Metals and Technology, Lepi pot 11, 1000 Ljubljana, Slovenia

ARTICLE INFO

Keywords:

Austenitic stainless steel
Powder bed fusion
Low-Temperature plasma nitriding
Wear and corrosion behaviour
Dislocation cell structure

ABSTRACT

Due to the limited wear and corrosion properties of the austenitic stainless steel AISI 316 L, some applications require the benefits of nitriding. The aim of this work was to investigate whether the same positive effect of nitriding could be obtained for 316 L that was additive manufactured using the laser powder-bed fusion process and further solution treated at 1060 °C for 30 min, low-temperature plasma nitrided at 430 °C or both. This study was designed to better understand the additive-manufactured and solution-treated microstructures as well as developing a nitride and a diffusion layer. The comparison of the wear and corrosion resistance, the micro-hardness and the microstructure changes of the additive-manufactured steel in different post-treated conditions with a commercial steel was carried out. It was found that the post-treated low-temperature plasma nitriding improves the wear and corrosion resistance of the additive-manufactured samples. The obtained values are similar to the values of conventionally fabricated and nitrided 316 L. The solution treating itself (without further nitriding) did not have any significant impact on these properties. It was possible to explain the microstructure at the nano level as well as correlating the wear and corrosion properties.

1. Introduction

Austenitic stainless steels are well known for their excellent corrosion resistance based on their high contents of chromium and nickel, which stimulate the formation of stable and passive oxide layers (Cr_2O_3) on the surface [1–3]. They represent one of the important grades of metallic materials implemented in various industrial applications, such as food and medical equipment, construction and others [4–6]. However, their poor mechanical properties (relatively low yield strength and low hardness) as well as moderate tribological properties (poor wear resistance) restrict their widespread use [2,7,8]. In order to improve their surface properties, many surface-treatment techniques, such as plasma or gas nitriding [9,10], magnetron sputtering [11] and ion implantation [12], were investigated. Plasma nitriding is one of the most common techniques, where two layers start to form on the surface. The thin compound layer contains ϵ (Fe_{2-3}N) and γ' (Fe_4N), as well as other nitrides formed with alloying elements [13–15]. The diffusion layer, formed beneath the compound layer, determines the strength. It consists of interstitial atoms in a solid solution, and if the solubility limit is reached, it also contains coherent nitride precipitates. A relatively thick diffusion layer is formed on the bcc structure, while on the

fcc structure this layer is much thinner [9].

During the low-temperature nitriding of austenitic stainless steel, expanded austenite is formed, which is responsible for the improved wear and corrosion resistance [16]. Expanded austenite is actually bcc austenite structure with atoms of nitrogen at interstitial positions. This expanded austenite is named the S phase and is formed up to 450 °C. On the other hand, the increase in nitriding temperature leads to the formation of CrN and a drop in the corrosion properties [17], as well as the transformation of the S phase to γ' (Fe_4N) [18].

Different grades of stainless steels, such as AISI 316 L, can be produced either by conventional manufacturing methods, such as casting, metal forming or powder metallurgy. Due to its relatively high machining costs and time-consuming procedures for fabricating accurate and complex structures there is an increasing interest in manufacturing 316 L components by additive manufacturing (AM). Austenitic stainless steels are some of the most suitable metallic materials for AM because there is no martensitic phase transformation and no precipitation during the rapid-solidification process, making them the most studied AM materials. AM is a rapidly developing technology that enables near-net-shape manufactured components and the enhancement of their properties [4,19]. For the manufacturing of engineering materials, of

* Corresponding author.

E-mail address: matjaz.godec@imt.si (M. Godec).

<https://doi.org/10.1016/j.addma.2019.101000>

Received 30 August 2019; Received in revised form 3 December 2019; Accepted 9 December 2019

Available online 11 December 2019

2214-8604/ © 2019 The Authors. Published by Elsevier B.V. This is an open access article under the CC BY-NC-ND license (<http://creativecommons.org/licenses/by-nc-nd/4.0/>).

particularly interest is selective laser melting (SLM), which is a powder-bed fusion process, characterized by the addition of a new component, layer by layer, using heat from a laser source [20].

A few years ago, the research related to AM was focused on the AM technology. However, investigations of the material properties, such as microstructure, mechanical and wear behaviour, corrosion resistance as well as comparisons of the properties of both conventionally and additive manufactured materials, have recently begun to emerge. Wang et al. [21] explained the hierarchical structure of the AM stainless steel 316 L, showing that the microstructure consists of nano dendrites, formed during rapid solidification, where the walls of these cells are built of dislocations. There are many nano oxides pinning the dislocations and therefore increasing the yield and tensile strengths without any loss of the elongation properties. Kurzynowski et al. [20] explained the relationship between the process parameters, microstructure and properties of AM-fabricated steel 316 L.

The tribological properties, such as wear resistance, are one of the key parameters of AM 316 L, and it was found that the wear resistance is worse than conventional 316 L due to the internal stresses [22]. The corrosion properties are also very important and are therefore often studied [23,24]. Some of the recent research [25,26] dealt with the positive effects of post-heat treatments on the wear and corrosion resistance of 316 L stainless steel produced by laser powder-bed fusion.

In the current research an attempt was made to achieve even better properties of the additive manufactured 316 L by post-treated, low-temperature plasma nitriding. For comparison reasons, a conventionally fabricated 316 L was nitrided under the same conditions. The microstructure, wear and corrosion resistance were analysed for both materials before and after the nitriding. Furthermore, the impact of a solution treatment on the wear and corrosion properties was investigated too.

2. Materials and methods

2.1. Materials

Commercial low-carbon austenitic stainless steel 316 L and AM-fabricated stainless steel 316 L are considered as the base materials for this research. Bulk wrought material produced with conventional manufacturing methods was delivered in the annealed condition. AM samples of $30 \times 30 \times 30 \text{ mm}^3$ were built in an industrial AM machine (EOS EOSINT M280) with 400-watt fibre laser, using the commercial process parameters of the powder-bed fusion process. The laser power was 285 W, and laser speed was 960 mm/s. The distance between the laser paths was 0.11 mm, with a laser diameter of 0.055 mm. The hatching occurred in the x and y directions, using alternating and rotating modes. The samples were fabricated in a nitrogen atmosphere of 99.5 % purity. The powder was supplied by LPW Technology Ltd, the size of the powder particles was 15–45 μm . The chemical compositions of the investigated materials (AM 316 L and wrought 316 L) are given in Table 1. The composition for AM 316 L corresponds to AM bulk material. The chemical composition determined by the standard (ASTM/ASME UNS S31603) is given for comparison.

Table 1

Chemical compositions of the investigated materials as well as standard values in wt. %, Fe balance.

	C	Si	Mn	Cr	Ni	Mo
AM 316 L	0.006	0.22	1.6	17.7	13.6	2.8
wrought 316 L	0.023	0.32	1.61	17.8	10.3	2.0
ASTM/ASME UNS S31603	0.03	< 0.75	< 2	16-18	10-14	2-3

Table 2

Labels and the sample conditions.

Label	Sample description
AM	AM 316 L as-built
AM + ST	AM 316 L as-built and solution treated (1060 °C, 30 min)
AM + N	AM 316 L as-built and nitrided (430 °C, 15 h)
AM + ST + N	AM 316 L as-built and solution treated and nitrided
316 L	Commercial 316 L as-delivered (wrought and heat treated)
316 L + N	Commercial 316 L as-delivered (wrought and heat treated) and nitrided

2.2. Heat treatment and low-temperature plasma nitriding

In order to improve the wear and corrosion properties, the AM-fabricated steel samples were post-treated by solution annealing, low-temperature plasma nitriding and a combination of both. Their properties were compared to commercial-grade counterparts. To eliminate the internal stresses and to homogenise the microstructure [27] some of the AM-fabricated samples were solution treated at 1060 °C for 30 min in a horizontal furnace and cooled in the air. Furthermore, the AM samples (as-built and solution treated) as well as commercial 316 L samples in the as-delivered state were low-temperature plasma nitrided. Before low-temperature plasma nitriding the samples' surfaces were ground with 1200-grit silicon carbide grinding paper and polished with a 1- μm diamond suspension to remove any surface deformations.

Low-temperature plasma nitriding was performed in a Metaplas Ionon HZIW 600/1000 reactor, equipped with a convection-heating system and an internal gas/water heat exchanger for rapid cooling. The convection and plasma heating of the specimens to the processing temperature took approximately 3.5 h. The soaking time at the nitriding temperature of 430 °C was 15 h. The specimens were nitrided in a 75 vol. % H₂:25 vol. % N₂ gas mixture. In Table 2, all the investigated samples are listed with their labels, used subsequently, and with a description of their conditions.

2.3. Microstructural evaluation

The nitrided samples were cut using a water-cooled saw in order to observe the nitride layer in cross-section. Afterwards, all the samples were mounted in conductive Bakelite resin, grinded and finally polished using 1- μm diamond suspension. The microstructures were analysed on the metallographic samples, etched by aqua regia (HNO₃ + 3 HCl) using a light microscope (Nikon Microphot FXA) equipped with a digital camera (Olympus DP73). In order to detect the ϵ and γ' phases on the nitrided samples, Marble etchant (4 g CuSO₄, 20 ml HCl, 20 ml H₂O) was used. Etching with Marble was used to define the ϵ and γ' phases. The ϵ phase is attacked by Marble and is seen as a dark layer, while the γ' is not etched by the Marble, and is observed as a white layer [28,29].

For the detailed microstructural investigation, a field-emission scanning electron microscope (ZEISS CrossBeam 550 FIBSEM) was used to perform analyses with energy-dispersive spectroscopy (EDS), electron-backscatter diffraction (EBSD) using a Hikari Super EBSD Camera to investigate the microstructure with included TEAM EDAX software and electron-channelling contrast imaging (ECCI). EBSD map analyses, as well as the secondary-electron imaging (SEI), were carried out at an accelerating voltage of 15 kV and probe currents of 5 nA and 2 nA, respectively.

ECCI is a SEM imaging technique in scanning electron microscopy based on the electron-channelling effect by applying a backscatter-electron detector. It is used for the direct observation of crystal defects, such as dislocations, cells and stacking faults close to the surface of bulk samples [30]. ECCI was performed using a backscattered detector (BSD) at various angles for an accelerating voltage of 30 kV, I probe of 2 nA.

Table 3
Parameters of reciprocating sliding-wear tests.

Counter body (32 mm)	100Cr6
Nominal load (N)	20
Sliding speed (m/s)	0.12
Amplitude (mm)	4
Frequency (Hz)	15
Test time (s)	833
Sliding distance (m)	100

2.4. Wear testing and hardness measurements

The AM samples in all conditions (AM, AM + ST, AM + N, AM + ST + N) as well as conventionally fabricated samples (316 L, 316 L + N) were subjected to reciprocating sliding-wear tests under atmospheric dry-sliding conditions with the ball-on-flat configuration to compare their wear resistance. The tests were performed at room temperature. A 32-mm-diameter 100Cr6 ball was used as the oscillating counter-body. Test parameters for the reciprocating sliding-wear tests are presented in Table 3. Three parallel tests were performed on all the samples. The wear resistance was plotted in terms of the wear volume, which was directly measured by analysing the wear track with an Alicona InfiniteFocus G4 3D optical microscope. It is a high-resolution 3D optical microscope based on a variation of the focus intended for topography and form measurements.

The Vickers microhardnesses $HV_{0.01}$ and bulk hardness HV_1 were measured on the metallographic samples using an Instron Tukon 2100 B Vickers hardness tester. The microhardness depth profile was

measured for the nitrided samples.

2.5. Electrochemical measurements

The surfaces of the solution-treated samples were ground and polished after heat treatment, prior to the electrochemical testing. The surfaces of the low-temperature, plasma-nitrided samples were ground and polished only prior to treatment, while the electrochemical testing was performed in the as-treated condition in order not to mechanically alter the surface after the nitriding.

The electrochemical experiments were carried out in a 3.5% NaCl solution. The solution was not deaerated. The measurements were performed using a three-electrode system, where the test specimen was employed as the working electrode (WE); the reference electrode (RE) was a saturated calomel electrode (SCE, 0.242 V vs. SHE); and the counter electrode (CE) was a platinum mesh. The potentiodynamic curves were recorded using a BioLogic® Modular Research Grade Potentiostat/Galvanostat/FRA Model SP-300 with EC-Lab® software V11.10., after 1 h of sample stabilization at the open-circuit potential (OCP), starting the measurement at 250 mV vs. SCE more negative than the OCP. The potential was then increased, using a scan rate of 1 mV/s. The corrosion current density (i_{corr}) and the corrosion rate (v_{corr}) were calculated according to ASTM G102 – 89 (2015) [31]:

$$v_{corr} = \frac{K\omega i_{corr}}{\rho}$$

where K is a conversion factor (3.27 mm·g/mA·cm·year), ω is the equivalent weight (g), ρ is the material density (g/cm³), and i_{corr} is the corrosion current density (mA/cm²). All the measurements were made

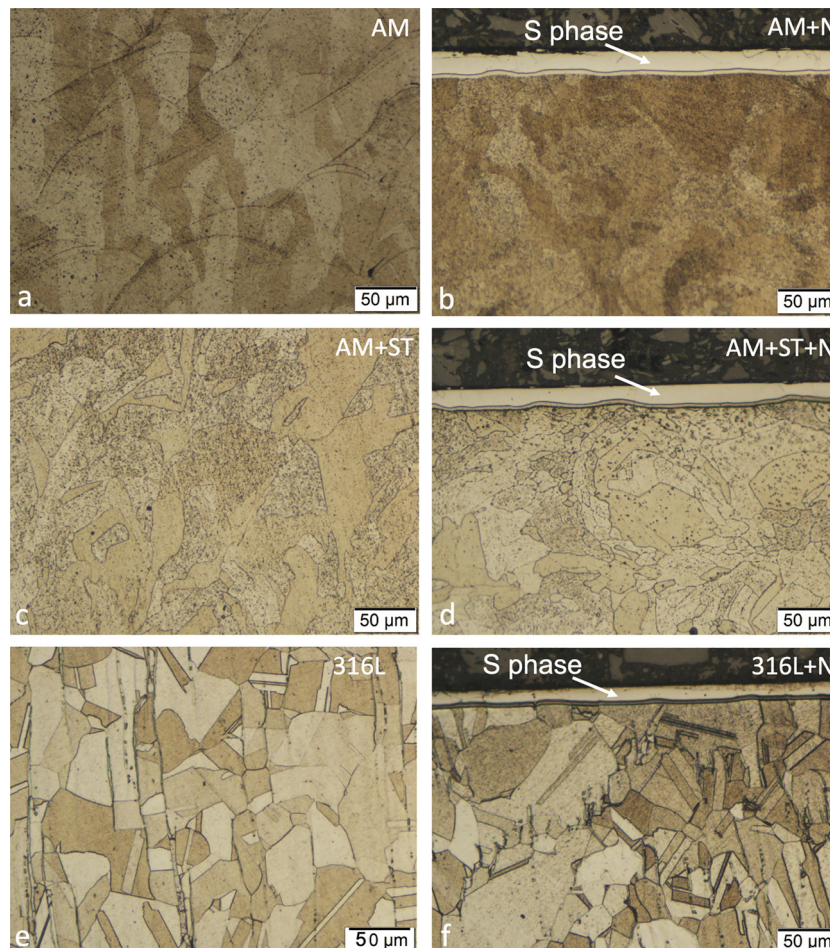


Fig. 1. Light micrographs of (a) AM, (b) AM + N, (c) AM + ST, (d) AM + ST + N, (e) 316 L and (f) 316 L + N samples.

at room temperature and were repeated three times. No larger discrepancies between the measurements were observed.

3. Results and discussion

AM metallic materials have a specific microstructure, defined by the laser powder-bed fusion process, known for its rapid solidification. Therefore, a lot of internal stress is accumulated in the structure, which is accommodated by the formation of dislocations [21,25]. Light micrographs show the well-known melt pools (Fig. 1a) caused by locally melted material. After a solution heat treatment, the metal pools are no longer visible and recrystallization takes place (Fig. 1c). Depending on the chosen nitriding parameters, ϵ and γ' phases or only the γ' or at lower temperature S phase forms on the sample surface. In the studied case only S phase with the thickness between 13 and 16 μm was formed on the surface, with a thin ($\sim 100 \mu\text{m}$) diffusion layer beneath (Fig. 1b, d and f). Below these phases is the diffusion zone, which is very thin in austenitic steel, compared to martensitic steel [32]. The dark layer on the top of these images is the Bakelite potting compound. Fig. 1e shows the typical microstructure of a commercial, conventionally manufactured 316 L, and in Fig. 1f with a nitride layer. Commercial, conventionally manufactured 316 L mostly consists of a small amount of δ ferrite phase, due to the segregation of Cr during the solidification. Due to the rapid solidification, which is typical for the AM SLM process, the formation of δ ferrite is not possible, while the AM DED (direct energy deposition) process sometimes leads to the δ ferrite phase [33]. The thin layer seen at the bottom of the nitride layer is attributed to the etching effect and the change in the chemical composition. The etched AM samples also show some small black spots, which are most probably due to the etching effect starting at certain lattice defects.

The EBSD IPF map of the AM sample shows a microstructure typical for AM metallic materials. The shapes of the grains do not follow exactly the shapes of the melt pools. Sometimes the grains grow through the melt-pool boundaries, and occasionally crystallisation starts at the bottom of the melt pool (Fig. 2a). The grains have a high misorientation

due to a slight rotation during the growth in order to compensate the stress. Depending on the AM parameters the structure can be more or less textured [20], as was the case in this experiment. The AM parameters also determine the porosity. The porosity of the investigated samples was estimated to be 0.3 %. It is assumed that after the solution treatment a partial recrystallization occurred with the grain growth (Fig. 2b). Chen et al. [4] studied the effect of annealing at different temperatures and reported that the grain size remains unchanged up to 800 $^{\circ}\text{C}$, although the EBSD images showed changes to the microstructure. In this study the average grain diameter of the AM sample was 8.3 μm , and after the solution treatment the grain size changed to 13.0 μm . This change in grain size is attributed to the higher annealing temperature (1060 $^{\circ}\text{C}$). The shape of the grains still tends to follow the melt-pool shapes, indicating that the recrystallization was not completed. Actually, the recrystallization is a consequence of extended sub-grain growth. This type of recrystallization has no proper nucleation process, but its growth process involves consuming dislocation structures. As a result, the long, extended sub-grain boundaries ending at the grain boundaries can be observed. At the same time the energetically favourable grains tend to grow, which results in slightly larger grains keeping the same melt-pool shapes while inside these grains the sub-grain structure is observed. No twin grain boundaries were found after the solution treatment, which also leads to the conclusion that the recrystallization of the grains is very limited. In the solution-treated sample the large misorientation is not so pronounced. In the larger grains there are substructures, i.e., areas with the same orientations. Commercial 316 L has a very similar grain size of the austenite phase to the solution-treated sample, i.e., 12.4 μm (Fig. 2c). The presence of δ ferrite was confirmed by the EBSD map.

ECCI is a technique that makes it possible to also observe dislocations in the SEM over a larger area. Fig. 3a shows the dendrite cell structure of 500-nm grain size, with the dendrites growing in the direction of the temperature gradient. Depending on the direction, more or less elongated cells can be observed. The cell walls are built from dislocations. The nano oxide particles are inside the cell walls and have

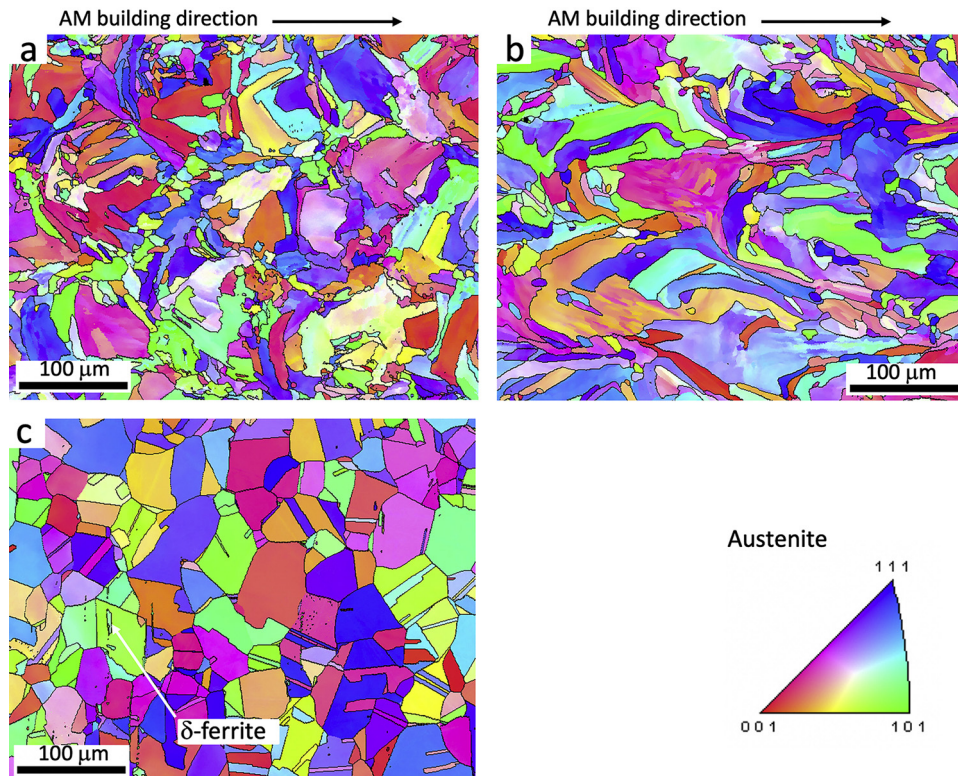


Fig. 2. EBSD IPF maps in the Z direction of (a) AM, (b) AM + ST and (c) 316 L samples.

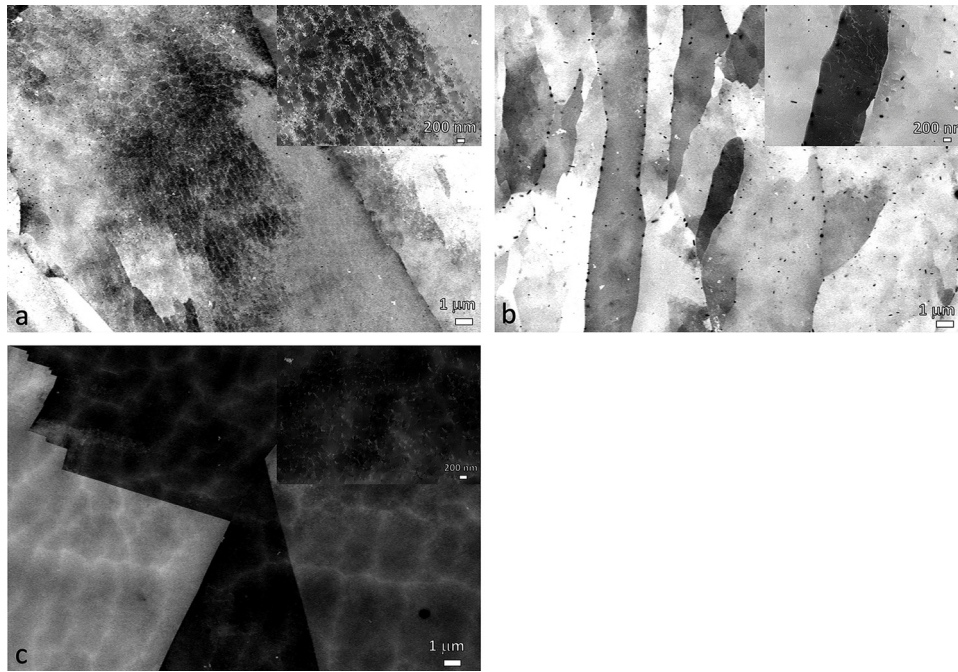


Fig. 3. ECCI images of (a) AM, (b) AM + ST, (c) 316 L samples with inserted details.

a size of 2–100 nm. In the literature [5,21,34] it was reported that these particles consist of Si and O. Due to the rapid solidification at the interdendritic locations the last solidified melt is rich in Mo and Cr [21]. After the solution treatment some of the oxide particles grow and others dissolve (Fig. 3b). The oxide particles mainly originate from a very thin oxide layer on each 316 L powder particle that was used as the starting material for the AM. The result is a new microstructure with larger and fewer oxide particles (50–500 nm) distributed along new, low-angle grain boundaries situated in the substructure, also observed in the EBSD map (Fig. 2b). However, a lot of oxide particles are still distributed within the grains. The dislocation density is significantly decreased and the dislocations are randomly distributed in the grains.

Fig. 3c shows the typical grain-boundary shape of austenitic steel with a similar dislocation density and distribution as we found in the AM and the solution-treated AM sample. The oxide particles are mostly not present, only those from the de-oxidation process of conventional steel production that are not trapped in the slag. The AM process does not allow the formation of MnS, whereas the solidification rate in the conventional process enables the precipitation and growth of MnS [35]. While the ECCI technique is sensitive to structural irregularities (dislocations) it is also very sensitive to differences in the chemical composition. Therefore, the white structure in Fig. 3c is observed, which originates from segregation during casting and was not completely removed during the subsequent plastic deformation process.

The SE images in Fig. 4 show cross-sections of the nitrified AM + N (Fig. 4a), AM + ST + N (Fig. 4c) and 316 L + N (Fig. 4d) samples. The nitride layer on the top consists of the S phase, and shows very little porosity and some cracks. Below the nitride layer is a 3–4- μm layer that etched differently to the bulk material due to its different chemical composition. During the nitriding process the nitrogen diffused beneath the nitride layer and formed a very thin diffusion layer, and some of the Cr is also depleted in this layer. The bulk etched sample shows dendritic cell structures, which are also visible in the ECCI images (Fig. 3a). These cell structures are actually nano-segregations of Mo and Cr. However, the segregation of Cr at the dislocation cell walls is so minor that it is insignificant to the corrosion resistance [21]. In the diffusion layer a similar cell-structure pattern as in the bulk can be observed (Fig. 4b). It is interesting that this cell-structure pattern can also be observed in the bottom part of the nitride layer. Diffusion during low-

temperature nitriding is not sufficient to eliminate the nano-segregations of Cr and Mo as well as the dislocation structures. The high-temperature (800 °C) stability of the dislocation cell structure was reported very recently [4]. The nitride layer on the AM sample has different properties (higher dislocation density) than the nitride layer on the solution-treated AM and conventional 316 L. This is not visible in the solution-treated sample because the cell structure changed, and partial recrystallization and grain growth occurred. The EDS line analyses in Fig. 4a, c and d show a slight depletion of Cr and an increase in the amount of nitrogen in the nitride layer. The peaks in the EDS line analysis in the nitride layer (Fig. 4a) showing an increase of Cr and N as well as the depletion of Fe are due to the very thin CrN layer. This phenomenon is observed only in the AM + N sample, while on AM + ST + N and 316 L + N no CrN precipitation takes place. It is assumed that a high stress and higher dislocation density influence the CrN precipitation along the austenite grain boundaries. The solution treatment of the AM sample reduces the stress and dislocation density and therefore impedes the CrN formation.

Below the nitride layer no significant decrease of Cr is detected. This is very important for the corrosion properties, while the stable Cr_2O_3 determines the corrosion properties of stainless steels. Although the slightly different chemical composition of the area below the nitride layer is the reason for the different chemical attack during etching, it is below the EDS detection limit. The nitrogen content rapidly decreases at the border of the nitride layer, and is still slightly decreasing below the nitride layer. This can be demonstrated using hardness measurements (Fig. 5).

The Vickers microhardnesses $\text{HV}_{0.01}$ of the nitride layer of the AM + N and AM + ST + N are 1454 and 1220, respectively (Fig. 5). The hardness of the nitride layer of the conventional 316 L + N is 1194, very similar to that of the AM + ST + N. The nitride layer of the AM + N material is much harder than the AM + ST + N due to the higher density of the dislocations and the stress accumulated in the layer and due to small amount of very hard CrN phase. At a depth of approximately 100 μm the hardness of the bulk is reached. The hardness of the bulk material in the case of 316 L is approximately 200 HV_1 . AM + ST material shows similar bulk hardness while AM has a higher bulk hardness of 260 HV_1 .

After 100 m of sliding against a hardened 100Cr6 steel ball bearing

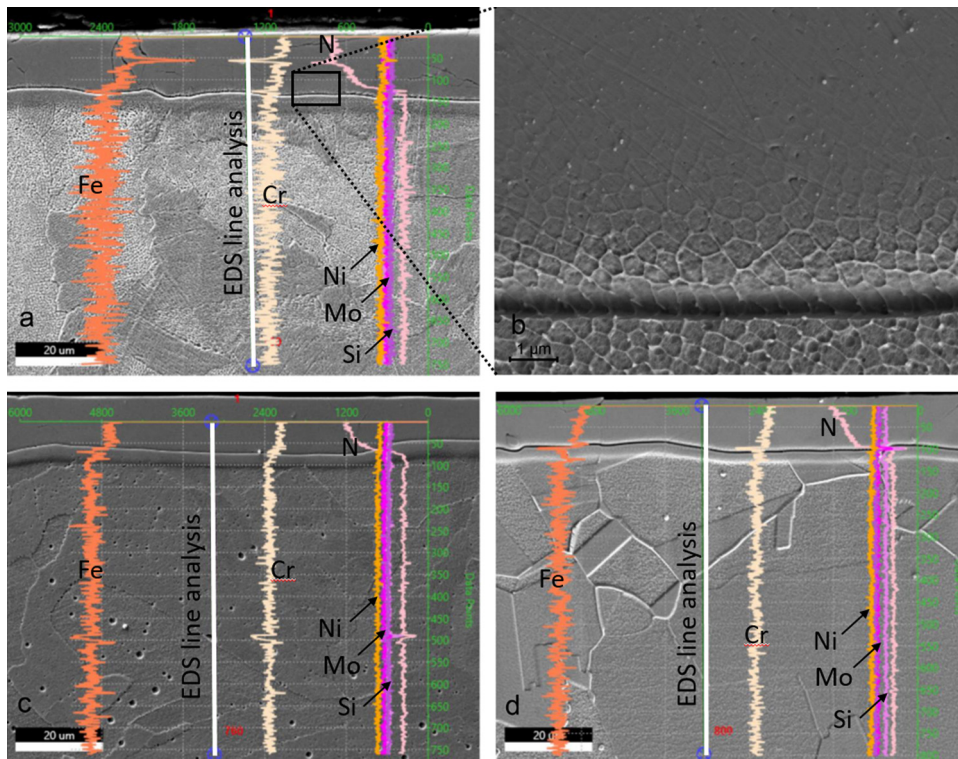


Fig. 4. SE images of (a) AM + N, (b) detail from fig. (a), (c) AM + ST, (d) 316L + N with EDS line analysis.

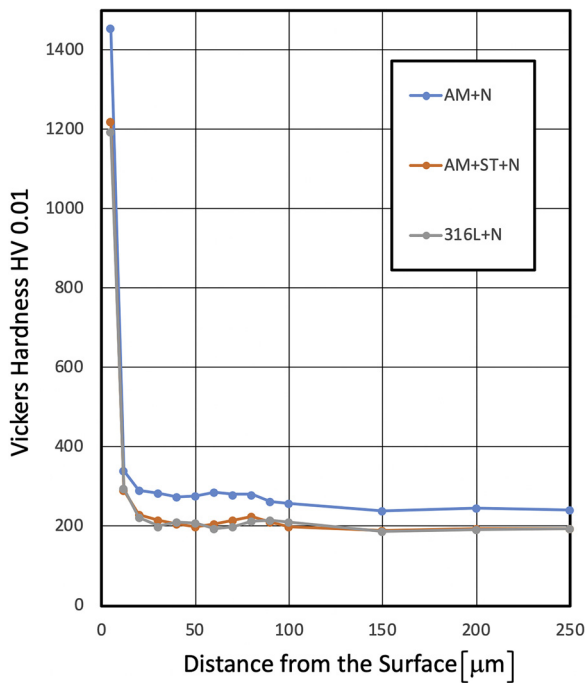


Fig. 5. Microhardness HV_{0.01} depth profile for nitrided samples.

the conventional 316L stainless steel displayed a combination of adhesive and abrasive wear (Fig. 6a), with the wear volume of $5.4 \cdot 10^{-2} \text{ mm}^3$ and steady-state coefficient of friction of 0.8, as shown in

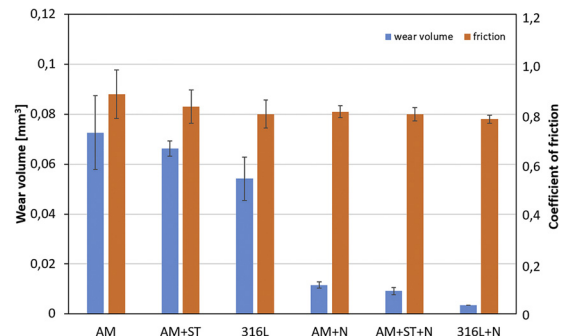


Fig. 7. Wear volume and coefficient of friction of the 100Cr6 counter-ball sliding against different austenitic stainless-steel samples.

Fig. 7. Switching to the AM material results in more pronounced abrasive wear component (Fig. 6b) with a higher friction (~ 0.87) as well as intensified wear, with the wear volume being increased to $7.2 \cdot 10^{-2} \text{ mm}^3$. The solution treatment of the AM material improved its wear resistance, especially the abrasive wear resistance, slightly reducing the friction and wear volume ($\sim 6.6 \cdot 10^{-2} \text{ mm}^3$), as well as the scatter of the experimental results. However, the tribological performance of the AM material is still inferior to conventional 316 L stainless steel. The improvement obtained by solution treatment could be due to lowering the dislocation density and eliminating the chemical nano segregation.

The main goal of nitriding is to improve the wear and corrosion resistance [9,36]. According to the wear measurements it is clear that nitriding improves the wear resistance and decreases the friction as well as the volume of lost material during the wear tests by almost an order



Fig. 6. Typical wear scars for (a) 316L, (b) AM and (c) AM + N.

of magnitude for all the investigated samples (Fig. 7). It also results in a predominantly abrasive wear mechanism (Fig. 6c). However, even after nitriding the conventional 316 L stainless steel displays much better wear resistance than the AM samples, with the wear volume of $0.3 \cdot 10^{-2} \text{ mm}^3$ as compared to $\sim 1.0 \cdot 10^{-2} \text{ mm}^3$ (Fig. 7).

For all cases, the AM material shows lower wear resistance as well as higher scatter. In general, higher hardness results in better wear resistance. However, this is only true for pure abrasive wear. In the case of combination of adhesive, abrasive and fatigue wear different properties become important, especially toughness of the material. In the present case of combined adhesive/abrasive wear mechanism the dominating wear resistance of the conventional 316 L, although showing slightly lower hardness can be attributed to larger grains, lower density of dislocations as well as to the presence of δ ferrite in the microstructure. It is well known that a small amount of δ ferrite improves mechanical properties [37], while an increase in grain size can have a positive effect on the wear resistance [38]. The same trend can be observed after the nitriding process, although for a much better wear resistance provided by increased compressive residual stresses [39]. The differences in the wear volumes of all the nitrided samples show that the nitride layer on the AM sample is slightly less wear resistant, most probably due to the high density of dislocations remaining after the nitriding. However, when analysing the depth of the nitriding layer remaining after the wear test all the specimens showed very similar results, with the thickness being in the range of $7 \mu\text{m}$.

Potentiodynamic polarization curves for the AM, AM + ST, AM + N, AM + ST + N, 316 L and 316 L + N samples performed in 3.5 % NaCl are shown in Fig. 8. The corrosion potentials (E_{corr}) in a 3.5 % NaCl solution for the AM, AM + ST, AM + N, AM + ST + N, 316 L and 316 L + N samples are approximately -160 mV , -143 mV , -114 mV , -250 mV , -241 mV and -187 mV vs. SCE, respectively (Table 4). After the Tafel region, the investigated samples exhibit a passive range, followed by the breakdown potential (E_b). Despite the high dislocation density and the chemical nano-segregations, the AM material has surprisingly good corrosion properties, as already noted in the literature data [3,40]. After a solution treatment (AM + ST) a decrease in the corrosion stability is observed due to the grain growth. Nitriding itself is actually expected to significantly improve the corrosion characteristics of the material. However, even a slight increase in the corrosion rate of the AM + N sample is observed compared to the AM sample. The reason is the formation of chromium nitrides (CrN) in the nitride layer which are known for their negative effect on the corrosion stability [17]. Furthermore, an improved corrosion resistance of the specimens after solution treatment and nitriding (AM + ST + N) is observed, which is manifested in a shift of the passivation range to significantly lower corrosion-current densities for the surface-treated samples [36].

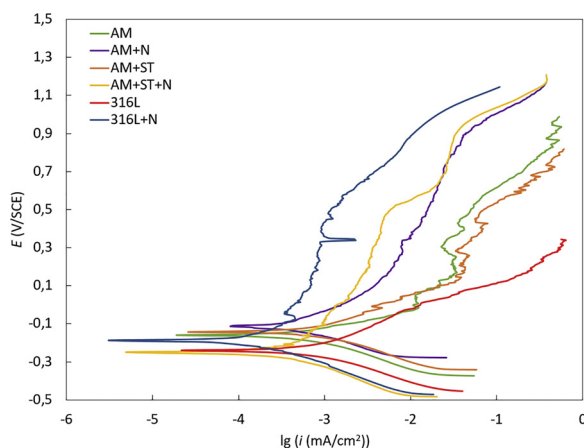


Fig. 8. Potentiodynamic curves for AM, AM + ST, AM + N, AM + ST + N, 316 L and 316 L + N in 3.5 % NaCl.

Table 4

Electrochemical parameters determined from the potentiodynamic measurements.

Sample	E_{corr} (mV)	i_{corr} ($\mu\text{A}/\text{cm}^2$)	v_{corr} ($\mu\text{m}/\text{year}$)
AM	-160 ± 6	0.63 ± 0.03	7.0 ± 0.3
AM + ST	-143 ± 5	0.96 ± 0.05	10.6 ± 0.4
AM + N	-114 ± 4	0.72 ± 0.04	7.7 ± 0.3
AM + ST + N	-250 ± 9	0.42 ± 0.02	4.7 ± 0.2
316 L	-241 ± 9	0.55 ± 0.03	10.5 ± 0.4
316 L + N	-187 ± 7	0.31 ± 0.01	3.5 ± 0.2

This improvement is attributed to the previous explained phenomena of the stress release by the solution treatment which impeded the formation of the CrN. The narrowest passive range is observed for a conventionally processed 316 L sample. Commercial 316 L also exhibits the highest corrosion rate, which can be explained by the presence of MnS and the associated Cr depletion in a conventionally processed stainless steel [41,42]. The corrosion parameters calculated from the potentiodynamic measurements also show decreased corrosion-current densities and corrosion rates for the 316 L + N specimen due to the improved barrier properties after nitriding (Table 4).

The influence of grain size on the corrosion resistance is difficult to generalize [43]. It is known that grain refinement, which alters the surface reactivity, influences the corrosion response. However, different factors such as chemical composition, environment and processing dictate the corrosion process leading to increased passivation or dissolution [43]. The grain refinement improves the formation of the passive layer due to the increased grain-boundary density and therefore improves the corrosion resistance. In this study, a slight increase in the corrosion rate for the AM samples was observed with an increase of the grain size after the solution treatment.

An additional factor that should be considered in terms of the corrosion performance is carbon content. Carbon stabilises the austenitic phase, but also has a negative effect on the corrosion properties due to the formation of chromium carbides [29]. However, it is generally recognised that a carbon content under 0.03 wt% prevents the formation of chromium carbides and therefore has no detrimental effect on the corrosion resistance of stainless steel [29], as was also observed in the present study.

Another important aspect that should be addressed in the present study is the influence of nitriding on the corrosion resistance of the investigated samples. Low-temperature nitriding is acknowledged as an effective technique to improve the surface hardness as well as the corrosion resistance of austenitic stainless steels. The improvement is associated with the formation of the S phase and the diffusion layer beneath. At low temperatures (under $400 \text{ }^\circ\text{C}$), the precipitation of chromium nitrides that are detrimental for corrosion resistance is avoided [17]. The observed CrN precipitation in the AM sample is not only the result of a slightly higher nitriding temperature ($430 \text{ }^\circ\text{C}$), but also of a high accumulated stress and a high dislocation density. This study leads to the conclusion that a solution treatment accompanied by further nitriding enables the optimal conditions regarding mechanical and corrosion properties.

4. Conclusions

A comparative study on the effect of the post-treated low-temperature plasma nitriding of AM and conventionally fabricated 316 L austenitic stainless steel on the wear and corrosion resistance as well as on the changes to the microstructure was conducted. The effect of the solution treatment on the AM material was also investigated. The study has led to the following conclusions:

- Nitriding under the same conditions leads to the formation of similar, between $13\text{--}16 \mu\text{m}$ -thick layers of S phase. The hardness

values of these layers are different depending on the hardness of the bulk material. The hardness of the AM material is higher due to the accumulated stresses and the consequently higher dislocation density and in some cases also due to precipitation of the hard CrN phase. The estimated thickness of the diffusion layer is approximately 100 μm , which is far less than in martensitic steels. Beneath the nitride layer no significant Cr depletion was observed, which is very important for good corrosion properties. The bottom part of the AM diffusion layer exhibits the same cell structure, which remains during the low-temperature nitriding process. This phenomenon is not seen in the solution-treated samples.

- The dislocation cell structure revealed by the ECCI technique is actually dendrites built from elongated nano cells, the walls of which are formed from dislocations. The elongated nano cells grow radially in the build direction due to the thermal gradient; however, some of them can grow perpendicular, depending on the locally disordered conditions.
- The dislocation density after the solution treatment is significantly decreased, while the dislocations are more-or-less randomly distributed in the grains. The solution treatment also leads to nano oxide growth, which is distributed along new high- and low-angle grain boundaries.
- The crystal grain shapes of the AM indicate the melt-pool shapes, and also after the solution treatment a partial recrystallization occurs and the grains grow slightly from 8.3 μm to 13.0 μm , with some weak melt-pool shapes still being observed. The misorientation inside the grains is diminished after the solution treatment, but some kind of substructure is observed resulting from the consuming of the dislocation structure.
- The wear volume of the solution-treated AM material is just slightly lower than the untreated material. After nitriding, the wear volume is significantly decreased, although it does not reach the value of the conventional fabricated material. The difference in the wear volume between the nitrided and the solution-treated plus nitrided AM material is almost negligible.
- The AM material in its as-built state exhibits better corrosion properties in comparison to its commercial counterpart. The solution treatment without further nitriding as well as nitriding without prior solution treatment of the AM material does not have any positive impact on the corrosion properties. Nevertheless, the superior corrosion properties are achieved by a combination of solution treatment and nitriding due to the prevention of CrN precipitation by eliminating stress and other lattice imperfections and are very similar to the corrosion properties of the nitrided commercial 316 L.

CRedit authorship contribution statement

M. Godec: Conceptualization, Investigation, Supervision, Writing - original draft. **Č. Donik:** Investigation. **A. Kocijan:** Investigation, Writing - review & editing. **B. Podgornik:** Investigation, Writing - review & editing. **D.A. Skobir Balantič:** Investigation, Writing - original draft.

Declaration of Competing Interest

None.

Acknowledgment

The authors acknowledge the financial support from the Slovenian Research Agency (research core funding Nos. P2-0132 and P2-0050).

References

- [1] F. Bottoli, M.S. Jellesen, T.L. Christiansen, G. Winther, M.A.J. Somers, High temperature solution-nitriding and low-temperature nitriding of AISI 316: effect on pitting potential and crevice corrosion performance, *Appl. Surf. Sci.* 431 (2018) 24–31, <https://doi.org/10.1016/j.apsusc.2017.06.094>.
- [2] J. Biehler, H. Hoche, M. Oechsner, Corrosion properties of polished and shot-peened austenitic stainless steel 304L and 316L with and without plasma nitriding, *Surf. Coatings Technol.* 313 (2017) 40–46, <https://doi.org/10.1016/j.surfcoat.2017.01.050>.
- [3] Q. Chao, V. Cruz, S. Thomas, N. Birbilis, P. Collins, A. Taylor, P.D. Hodgson, D. Fabijanic, On the enhanced corrosion resistance of a selective laser melted austenitic stainless steel, *Scr. Mater.* 141 (2017) 94–98, <https://doi.org/10.1016/j.scriptamat.2017.07.037>.
- [4] N. Chen, G. Ma, W. Zhu, A. Godfrey, Z. Shen, G. Wu, X. Huang, Enhancement of an additive-manufactured austenitic stainless steel by post-manufacture heat-treatment, *Mater. Sci. Eng. A.* 759 (2019) 65–69, <https://doi.org/10.1016/j.msea.2019.04.111>.
- [5] K. Saeidi, X. Gao, Y. Zhong, Z.J. Shen, Hardened austenite steel with columnar sub-grain structure formed by laser melting, *Mater. Sci. Eng. A.* 625 (2015) 221–229, <https://doi.org/10.1016/j.msea.2014.12.018>.
- [6] Y. Zhong, L. Liu, S. Wikman, D. Cui, Z. Shen, Intragranular cellular segregation network structure strengthening 316L stainless steel prepared by selective laser melting, *J. Nucl. Mater.* 470 (2016) 170–178, <https://doi.org/10.1016/j.jnucmat.2015.12.034>.
- [7] X. Qin, X. Guo, J. Lu, L. Chen, J. Qin, W. Lu, Erosion-wear and intergranular corrosion resistance properties of AISI 304L austenitic stainless steel after low-temperature plasma nitriding, *J. Alloys. Compd.* 698 (2017) 1094–1101, <https://doi.org/10.1016/j.jallcom.2016.12.164>.
- [8] H. Zhang, H. Qin, Z. Ren, J. Zhao, X. Hou, G.L. Doll, Y. Dong, C. Ye, Low-temperature nitriding of nanocrystalline Inconel 718 alloy, *Surf. Coatings Technol.* 330 (2017) 10–16, <https://doi.org/10.1016/j.surfcoat.2017.09.040>.
- [9] V. Leskovšek, M. Godec, P. Kogej, Low temperature nitriding of strain induced martensite and laser quenched austenite, in: *23rd Int. Fed. Heat Treat. Surf. Eng. Congr.* 2016 (2016) IFHTSE 2016.
- [10] L.C. Gontijo, R. Machado, S.E. Kuri, L.C. Casteletti, P.A.P. Nascente, Corrosion resistance of the layers formed on the surface of plasma-nitrided AISI 304L steel, *Thin Solid Films* 515 (2006) 1093–1096, <https://doi.org/10.1016/j.tsf.2006.07.075>.
- [11] A. Saker, C. Leroy, H. Michel, C. Frantz, Properties of sputtered stainless steel-nitrogen coatings and structural analogy with low temperature plasma nitrided layers of austenitic steels, *Mater. Sci. Eng. A.* 140 (1991) 702–708, [https://doi.org/10.1016/0921-5093\(91\)90500-M](https://doi.org/10.1016/0921-5093(91)90500-M).
- [12] G.A. Collins, R. Hutchings, K.T. Short, J. Tendys, X. Li, M. Samandi, Nitriding of austenitic stainless steel by plasma immersion ion implantation, *Surf. Coatings Technol.* 74–75 (1995) 417–424, [https://doi.org/10.1016/0257-8972\(95\)08370-7](https://doi.org/10.1016/0257-8972(95)08370-7).
- [13] Z.L. Zhang, T. Bell, Structure and corrosion resistance of plasma nitrided stainless steel, *Surf. Eng.* 1 (1985) 131–136.
- [14] M.G. Shahri, M. Salehi, S.R. Hosseini, M. Naderi, Effect of nanostructured grains on martensite formation during plasma nitriding of AISI 321 austenitic stainless steel, *Surf. Coatings Technol.* 310 (2017) 231–238, <https://doi.org/10.1016/j.surfcoat.2016.12.019>.
- [15] E. Boztepe, A.C. Alves, E. Ariza, L.A. Rocha, N. Cansever, F. Toptan, A comparative investigation of the corrosion and tribocorrosion behaviour of nitrocarburized, gas nitrided, fluidized-bed nitrided, and plasma nitrided plastic mould steel, *Surf. Coatings Technol.* 334 (2018) 116–123, <https://doi.org/10.1016/j.surfcoat.2017.11.033>.
- [16] J. Buhagiar, H. Dong, Corrosion properties of S-phase layers formed on medical grade austenitic stainless steel, *J. Mater. Sci. Med.* 23 (2012) 271–281, <https://doi.org/10.1007/s10856-011-4516-z>.
- [17] B. Larisch, U. Brusky, H.J. Spies, Plasma nitriding of stainless steels at low temperatures, *Surf. Coat. Technol.* 116 (1999) 205–211, [https://doi.org/10.1016/S0257-8972\(99\)00084-5](https://doi.org/10.1016/S0257-8972(99)00084-5).
- [18] L.C. Gontijo, R. Machado, E.J. Miola, L.C. Casteletti, N.G. Alcantara, P.A.P. Nascente, Study of the S phase formed on plasma-nitrided AISI 316L stainless steel, *Mater. Sci. Eng. A-STRUCTURAL Mater. Prop. Microstruct. Process.* 431 (2006) 315–321, <https://doi.org/10.1016/j.msea.2006.06.023>.
- [19] D. Kong, C. Dong, X. Ni, L. Zhang, J. Yao, C. Man, X. Cheng, K. Xiao, X. Li, Mechanical properties and corrosion behavior of selective laser melted 316L stainless steel after different heat treatment processes, *J. Mater. Sci. Technol.* 35 (2019) 1499–1507, <https://doi.org/10.1016/j.jmst.2019.03.003>.
- [20] T. Kurzynowski, K. Gruber, W. Stopyra, B. Kuznicka, E. Chlebus, Correlation between process parameters, microstructure and properties of 316 L stainless steel processed by selective laser melting, *Mater. Sci. Eng. A-STRUCTURAL Mater. Prop. Microstruct. Process.* 718 (2018) 64–73, <https://doi.org/10.1016/j.msea.2018.01.103>.
- [21] Y.M. Wang, T. Voisin, J.T. McKeown, J. Ye, N.P. Calta, Z. Li, Z. Zeng, Y. Zhang, W. Chen, T.T. Roehling, R.T. Ott, M.K. Santala, P.J. Depond, M.J. Matthews, A.V. Hamza, T. Zhu, Additively manufactured hierarchical stainless steels with high strength and ductility, *Nat. Mater.* 17 (2018) 63–70, <https://doi.org/10.1038/NMAT5021>.
- [22] F. Bartolomeu, M. Buciumeanu, E. Pinto, N. Alves, O. Carvalho, F.S. Silva, G. Miranda, 316L stainless steel mechanical and tribological behavior—a comparison between selective laser melting, hot pressing and conventional casting, *Addit. Manuf.* 16 (2017) 81–89, <https://doi.org/10.1016/j.addma.2017.05.007>.
- [23] M.J.K. Lodhi, K.M. Deen, M.C. Greenlee-Wacker, W. Haider, Additively manufactured 316L stainless steel with improved corrosion resistance and biological response for biomedical applications, *Addit. Manuf.* 27 (2019) 8–19, <https://doi.org/10.1016/j.addma.2019.02.005>.
- [24] A.H. Etefagh, S. Guo, Electrochemical behavior of AISI316L stainless steel parts

[1] F. Bottoli, M.S. Jellesen, T.L. Christiansen, G. Winther, M.A.J. Somers, High

- produced by laser-based powder bed fusion process and the effect of post annealing process, *Addit. Manuf.* 22 (2018) 153–156, <https://doi.org/10.1016/j.addma.2018.05.014>.
- [25] C. Elangeswaran, A. Cutolo, G.K. Muralidharan, C. de Formanoir, F. Berto, K. Vanmeensel, B. Van Hooreweder, Effect of post-treatments on the fatigue behaviour of 316L stainless steel manufactured by laser powder bed fusion, *Int. J. Fatigue* 123 (2019) 31–39, <https://doi.org/10.1016/j.ijfatigue.2019.01.013>.
- [26] Y. Kaynak, O. Kitay, The effect of post-processing operations on surface characteristics of 316L stainless steel produced by selective laser melting, *Addit. Manuf.* 26 (2019) 84–93, <https://doi.org/10.1016/j.addma.2018.12.021>.
- [27] F. Yan, W. Xiong, E. Faierson, G.B. Olson, Characterization of nano-scale oxides in austenitic stainless steel processed by powder bed fusion, *Scr. Mater.* 155 (2018) 104–108, <https://doi.org/10.1016/j.scriptamat.2018.06.011>.
- [28] George F. Vander Voort, *Metallography Principles and Practice*, McGraw-Hil, (1984).
- [29] J.R. Davis (Ed.), *ASM Specialty Handbook: Stainless Steels*, ASM International, 1994.
- [30] S. Zaefferer, N.-N. Elhami, Theory and application of electron channelling contrast imaging under controlled diffraction conditions, *Acta Mater.* 75 (2014) 20–50, <https://doi.org/10.1016/j.actamat.2014.04.018>.
- [31] ASTM G102 – 89, (2015) *Standard Practice For Calculation Of Corrosion Rates And Related Information From Electrochemical Measurements*, (2015).
- [32] V. Leskovsek, M. Godec, P. Kogej, Influence of low-temperature nitriding on the strain-induced martensite and laser-quenched austenite in a magnetic encoder made from 304L stainless steel, *Sci. Rep.* 6 (2016), <https://doi.org/10.1038/srep30979>.
- [33] A. Yadollahi, N. Shamsaei, S.M. Thompson, D.W. Seely, Effects of process time interval and heat treatment on the mechanical and microstructural properties of direct laser deposited 316L stainless steel, *Mater. Sci. Eng. A-STRUCTURAL Mater, Prop. Microstruct. Process.* 644 (2015) 171–183, <https://doi.org/10.1016/j.msea.2015.07.056>.
- [34] K. Saeidi, X. Gao, F. Lofaj, L. Kvetková, Z.J. Shen, Transformation of austenite to duplex austenite-ferrite assembly in annealed stainless steel 316L consolidated by laser melting, *J. Alloys. Compd.* 633 (2015) 463–469, <https://doi.org/10.1016/j.jallcom.2015.01.249>.
- [35] M. Suzuki, R. Yamaguchi, K. Murakami, M. Nakada, Inclusion particle growth during solidification of stainless steel, *ISIJ Int.* 41 (2001) 247–256, <https://doi.org/10.2355/isijinternational.41.247>.
- [36] H.-J. Spies, 6 - Corrosion behaviour of nitrided, nitrocarburised and carburised steels, in: E.J. Mittemeijer, M.A.J. Somers (Eds.), *Thermochem. Surf. Eng. Steels*, Woodhead Publishing, Oxford, 2015, pp. 267–309, <https://doi.org/10.1533/9780857096524.2.267>.
- [37] A. Gigovic-Gekic, M. Oruc, H. Avdusinovic, R. Sunulahpasic, Regression analysis of the influence of a chemical composition on the mechanical properties of the Steel Nitronic 60, *Mater. Tehnol.* 48 (2014) 433–437.
- [38] L. Zhou, G. Liu, Z. Han, K. Lu, Grain size effect on wear resistance of a nanostructured AISI52100 steel, *Scr. Mater.* 58 (2008) 445–448, <https://doi.org/10.1016/j.scriptamat.2007.10.034>.
- [39] S. Jegou, L. Barrallier, R. Kubler, Residual stress development during nitriding of steels, in: P. Scardi, C.L.A. Ricardo (Eds.), *RESIDUAL Stress. VIII*, 2011, pp. 370–373, <https://doi.org/10.4028/www.scientific.net/MSF.681.370>.
- [40] Y. Zhang, J. Zhang, Q. Yan, L. Zhang, M. Wang, B. Song, Y. Shi, Amorphous alloy strengthened stainless steel manufactured by selective laser melting: enhanced strength and improved corrosion resistance, *Scr. Mater.* 148 (2018) 20–23, <https://doi.org/10.1016/j.scriptamat.2018.01.016>.
- [41] M.P. Ryan, D.E. Williams, R.J. Chater, B.M. Hutton, D.S. McPhail, Why stainless steel corrodes, *Nature.* 415 (2002) 770–774, <https://doi.org/10.1038/415770a>.
- [42] D.E. Williams, M.R. Kilburn, J. Clifff, G.I.N. Waterhouse, Composition changes around sulphide inclusions in stainless steels, and implications for the initiation of pitting corrosion, *Corros. Sci.* 52 (2010) 3702–3716, <https://doi.org/10.1016/j.corsci.2010.07.021>.
- [43] K.D. Ralston, N. Birbilis, Effect of grain size on corrosion: a review, *Corrosion* 66 (2010), <https://doi.org/10.5006/1.3462912>.